GEOPHYSICS, VOL. 80, NO. 5 (SEPTEMBER-OCTOBER 2015); P. L57–L72, 15 FIGS.
10.1190/GEO2014-0532.1

Experimental study of Young's modulus dispersion and attenuation in fully saturated sandstones

Lucas Pimienta[1], Jérôme Fortin[1], and Yves Guéguen[1]

ABSTRACT

Although seismic wave dispersion and attenuation have been found to occur in sedimentary rocks, it remains challenging to experimentally observe these effects. A new experimental setup has been developed to measure the Young's modulus and Poisson's ratio of rocks over a wide range in pressure ($P_c \in [0; 30]$ MPa) and frequency ($f \in [5.10^{-3}; 10^2]$ Hz). Calibration with standard samples determined the following: (1) no dependence of the apparatus to pressure and frequency and (2) a good fit between published data and the measured and inferred elastic properties. The measured Young's modulus dispersion and attenuation of Plexiglas were also consistent with the published data. The Young's modulus and the attenuation of Fontainebleau sandstone samples saturated by water and glycerin were then measured. Although small variations were observed for one sample, the second one exhibited strong pressure- and frequency-dependent variations of Young's modulus and attenuation. A frequency-dependent fluid flow was simultaneously measured. The characteristic frequency for these variations was highly fluid dependent. Accounting for the in situ fluids' viscosity using an apparent frequency parameter, we determined the Young's modulus and attenuation of a fluid-saturated Fontainebleau sandstone over an apparent frequency band of $f^* \in [10^{-3}; 10^5]$ Hz. The measurements under water and glycerin saturation compared favorably, and two frequency-dependent phenomena were observed that were interpreted as the drained/undrained and undrained/unrelaxed transitions. The undrained/unrelaxed transition occurred in a large frequency range, which was attributed to a distribution in aspect ratio of the rock's microcracks.

INTRODUCTION

Sedimentary rocks saturated by fluids are known to be dispersive materials. Their frequency-dependent behaviors originate from fluid movements in the rock's porous network induced by the elastic waves. When comparing field and laboratory measurements, the frequency dependence of the elastic properties is to be considered. For fully saturated rocks, two transitions between three elastic domains are expected (e.g., Cleary, 1978; Sarout, 2012) in the frequency range of interest (i.e., $f \in [10^{-1}; 10^6]$ Hz). The first transition is that from drained to undrained regimes. Both regimes are within the field of poroelasticity. This transition is expected to occur at low frequencies. The second transition, occurring at a higher frequency, is that from relaxed to unrelaxed regimes. This last situation is out of the validity domain of poroelasticity because the representative elementary volume (REV) is not in an isobaric state anymore.

Owing to the experimental complexities, very few laboratory apparatuses allow for measuring such frequency-dependent transitions. The stress-strain method is promising because it allows for measurement of elastic properties over wide frequency and pressure ranges up to about $f \in [10^{-3}; 10^3]$ Hz and $P_c \in [0; 100]$ MPa, respectively (e.g., Subramaniyan et al., 2014). Apparatuses for measurements of confining pressure (Adelinet et al., 2010; David et al., 2013; Fortin et al., 2014; Pimienta et al., 2015) or shear stress (e.g., Jackson and Paterson, 1987) oscillations have been developed, but the stress-strain method applied to axial stress oscillations is by far the most used (e.g., Batzle et al., 2001, 2006; Adam et al., 2006; Mikhaltsevitch et al., 2011; Tisato and Madonna, 2012; Madonna and Tisato, 2013). To the authors' knowledge, data from the literature, however, do not report clear transitions between the expected elastic regimes. First, the boundary conditions are chosen most of the time so that the fluid-saturated medium's elastic properties are directly undrained, thus discarding the transition from drained to

Manuscript received by the Editor 14 November 2014; revised manuscript received 9 April 2015; published online 12 August 2015.
[1]PSL Research University, Laboratoire de Géologie de l'ENS, Paris, France. E-mail: pimienta@geologie.ens.fr; fortin@geologie.ens.fr; guéguen@geologie.ens.fr.

undrained regimes. Second, a clear transition from undrained to unrelaxed domain is yet to be clearly reported.

Using three standard samples, this work reports a new experimental setup allowing for measuring frequency-dependent Young's modulus, Poisson's ratio, and Young's attenuation in the frequency and pressure ranges of $f \in [5.10^{-3}; 10^{2}]$ Hz and $P_c \in [0; 30]$ MPa, respectively. Young's modulus and its intrinsic attenuation are measured as a function of pressure and frequency on two Fontainebleau sandstone samples saturated by water and glycerin. Simultaneously, hydraulic properties are measured. The results are interpreted in the light of the usual fluid-flow theories and using published results on the bulk modulus of the same rock samples (Pimienta et al., 2015).

EXPERIMENTAL APPARATUS AND SAMPLES STUDIED

Samples studied

Calibration samples

Three standard samples were chosen to test the experimental setup and procedure: (1) a synthetic glass sample made of amorphous silica (Mallet et al., 2013, 2015), (2) a pure gypsum sample (Brantut et al., 2012), and (3) a Plexiglas (PMMA) sample (e.g., Batzle et al., 2006). These samples were chosen because (1) they are homogeneous and isotropic media at the sample scale, (2) their static and dynamic elastic properties are known, and they show a large range in elastic moduli, (3) these samples have no porosity, and their elastic properties are not expected to change with confining pressure or added axial stress, and (4) although glass and gypsum elastic properties are independent of frequency, Plexiglas is a viscoelastic material whose elastic properties are frequency dependent. Plexiglas is often used as a mean to test an attenuation apparatus (e.g., Batzle et al., 2006; Tisato and Madonna, 2012; Madonna and Tisato, 2013; Pimienta et al., 2015).

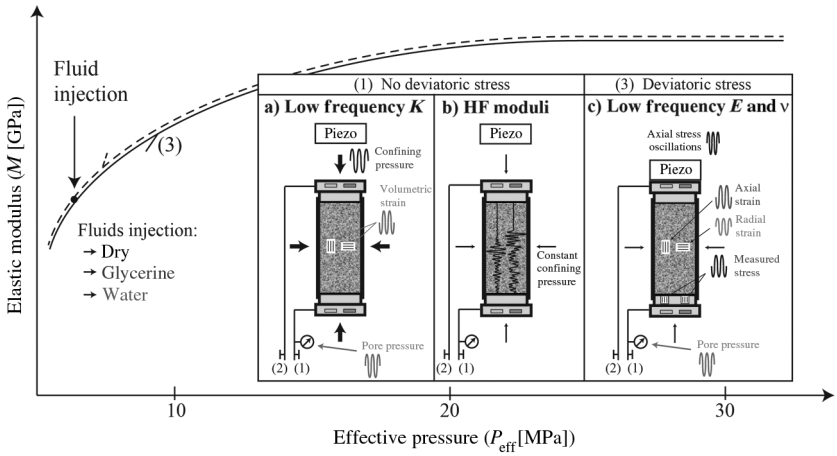

Figure 1. Schematic view of the experimental setup and procedure for measuring the whole set of (b) HF and (a and c) LF elastic moduli under different fluids' saturation. (1) Under no deviatoric stress, (a) LF confining pressure oscillations lead to measuring bulk modulus and (b) ultrasonic velocities are measured to infer the HF moduli. Under a small deviatoric stress, LF deviatoric oscillations are applied to measure Young's modulus and Poisson's coefficient. The cylindrical sample is isolated laterally from the confining oil using a rubber jacket.

Fontainebleau sandstone

Fontainebleau sandstone is a well-known reference rock. The framework grains and cement are pure quartz, making up a clean sandstone of approximately 99.9% qtz (Bourbie and Zinszner, 1985; Gomez et al., 2010). Because the rock was formed from deposited aeolian quartz grains, the rock possesses a random grain orientation and is well sorted with an average grain size of approximately 200 μm. The rock can consistently be assumed homogeneous and isotropic at the REV scale (i.e., volume ≫ grains' volume).

Depending on the amount of cementing quartz, Fontainebleau sandstone samples' porosity ranges from about $\phi \sim 2\%$ for highly cemented samples to about $\phi \sim 25\%$ for ill-cemented samples (e.g., Pimienta et al., 2014). The main differences between samples are the pores' entry diameters. These diameters decrease from $d \sim 20$ μm (high porosity) to about $d \sim 5$ μm (low porosity), which leads to variations in permeability of approximately 4–5 orders of magnitude (Bourbie and Zinszner, 1985). The two samples used in this study have, respectively, porosities of approximately $\phi \sim 7.3\%$ (i.e., Fo7) and $\phi \sim 8.3\%$ (i.e., Fo8), and they originate from the same blocks as in Pimienta et al. (2015). The samples are cored as cylinders of 40 mm diameter and rectified to 80 mm length with an accuracy of approximately 10 μm. Their total pore volume, measured from total fluid injection at lowest effective pressure, is, respectively, of $V_{Fo7} \sim 7.2$ mL and $V_{Fo8} \sim 8.2$ mL. This is consistent with the samples' dimensions of 40 mm diameter and 80 mm length, i.e., a rock volume of approximately 100 mL.

Experimental apparatus and procedure

Cell and confining setup

The apparatus aims at measuring simultaneously the complete set of elastic properties at high frequency (HF) and at low frequency (LF). To investigate these properties at different pressures, measurements are conducted in an oil-confining triaxial apparatus (Fortin et al., 2005). The sample is radially enclosed in a rubber jacket to be separated from the confining medium (i.e., oil). This oil-confining triaxial apparatus can be used in two different setups thanks to an axial piston that can be shifted vertically (Figure 1).

In the first setup, the axial piston is not in contact with the end platen (and thus the sample), allowing for studying the sample under pure isotropic conditions. As shown previously (Pimienta et al., 2015), this setup allows us to measure (1) LF bulk modulus K_{LF} and attenuation Q_K^{-1} using confining pressure oscillations (Figure 1a) at different frequencies and (2) ultrasonic P- and S-wave velocities (i.e., V_P and V_S) traveling through the sample (Figure 1b).

A second setup has been built to apply a deviatoric stress (Fortin et al., 2005). It is used to measure the LF Young's modulus E_{LF} and Poisson's ratio ν_{LF} using axial stress oscillations (Figure 1c) as a function of frequency. This second setup is the focus of the present contribution. As shown from the schematics (Figure 1), in

order to exert axial stress oscillations $\Delta\sigma_{ax}$ on the sample, an added deviatoric load σ^0_{ax} is needed to ascertain the stability of the measuring setup. Yet, the magnitude of σ^0_{ax} may affect the sample's properties during the measurement. The effect of this added deviatoric load is further investigated below, prior to introducing the measurements under fluid-saturated conditions.

Pore fluid setup

Pore pressure is controlled externally, and independently of the confining pressure, by a pair of connected *Quizix* servo pumps. The pore volume and pressure measurements accuracies are, respectively, of about $V_p \sim 0.1$ μL and $P_p \sim 0.001$ MPa. In addition, another pressure transducer of $P_p \sim 0.001$ MPa accuracy is placed near the sample. Valves are placed at both ends of the sample (Figure 1) to decrease as much as possible the pipes' dead volumes, and the pressure sensor is placed near the bottom end platen (i.e., inside the dead volume). The measured dead volumes are $V_{d1} = 3.433$ mL and $V_{d2} = 3.205$ mL, leading to a total dead volume of $V_d \sim 6.6$ mL, a value close to the total pore volume of each sample.

The valves can either be open or closed. The first configuration is chosen when changing the confining pressure, so that the fluid is kept at a constant pressure of $P_p = 2$ MPa, and the sample is drained during the pressure ramps. Following similar measurements (e.g., Batzle et al., 2006; Tisato and Madonna, 2012; Madonna and Tisato, 2013; Mikhaltsevitch et al., 2014; Pimienta et al., 2015), the second configuration is chosen, and the valves are closed during the axial stress oscillation $\Delta\sigma_{ax}$. In this configuration, the fluid mass is kept constant in the system (i.e., sample + dead volume). This system is experimentally undrained, and fluid pressure changes are tracked by the pore pressure sensor in the dead volume. This configuration was found to be the most appropriate because it discards any possible bias from an extrinsically induced differed fluid flow, i.e., from the delayed regulation of the pore pressure pump. Owing to the existence of the large dead volume and the sample's intrinsic storage capacity (e.g., Ghabezloo and Sulem, 2010), the samples used prove to remain drained under quasi-static conditions (Pimienta et al., 2015).

Low frequency setup

As discussed earlier, the LF measurements rely on the stress-strain method. An axial stress oscillation at a given frequency is applied to the sample, thus inducing a strain oscillation. The axial stress is exerted by a *PI* piezoelectric actuator scheduled to function in the range of $f \in [10^{-3}; 10^{2}]$ Hz and electric amplitudes of $A \in [10; 1000]$ V, with a maximum displacement of 30 μm. The oscillator is linked to (1) a LF generator sending a continuous sinusoidal electric signal of given amplitude (i.e., $A \in [0.1; 10]$ V) and frequency (i.e., $f \in [10^{-3}; 10^{8}]$ Hz) and (2) an amplifier. This actuator transforms a volt amplitude in a mechanical displacement, which directly depends on the sample's stiffness. Thus, stress cannot be directly inferred from the input voltage and is a function of the sample's strain.

To precisely measure the stress applied on the sample, two axial *FCB* 350 Ω strain gauges (*Tokyo Sokki* TML, FCB-6-350-11) of 6 mm length are glued to the aluminum bottom end platen. Stress is deduced by knowing the end platen Young's modulus; i.e., $E_0 = 72.5$ GPa. To measure the sample's strains, three pairs of axial and radial *FCB* 350 Ω strain gauges of 6 mm length are directly glued on the sample. All the strain gauges used are the same and are mounted in a one-fourth Wheatstone bridge, allowing us to discard possible bias by using different gauges (e.g., Adam et al., 2006). All strains and the pore pressure oscillations are transformed from electric to strain and pressure signals using Catman software and MGCplus recording system (HBM Inc.), able to record at frequencies up to 2400 Hz.

Experimental procedure

A procedure (Figure 1) is devised to measure the frequency and pressure dependence of the whole set of elastic moduli of rocks saturated by different fluids. Starting from an effective pressure of about $P_{eff} \sim 1$ MPa, the frequency dependence of the properties is measured at each confining pressure step up to the maximum confining of $P_{eff} = 30$ MPa. When changing the confining pressure, a controlled rate of about 0.01 MPa/s is used to allow for complete/instantaneous relaxation of the fluid-filled sample (Fortin et al., 2007). The same procedure is followed for the three different saturating conditions, such as, (1) dry, (2) water, and (3) glycerin saturation. For the sandstone samples in fluid saturated conditions, Terzaghi effective pressure $P_{eff} = P_c - P_p$ is used that allows for an approximate yet simple comparison between dry- and fluid-saturated conditions.

The glycerin full saturation is ascertained by a precise injection procedure: (1) vacuum is applied with a vacuum pump at the sample upper end until the measured P_p (at the sample's bottom) reaches a stable negative value of approximately −0.8 MPa and (2) then, the fluid is injected at the sample bottom although maintaining the vacuum with the vacuum pump. This injection procedure (using the vacuum pump) complements the density effect (i.e., air pushed up by the denser fluid) and was shown to allow for a 100% fluid saturation (e.g., Pimienta et al., 2015). Water saturation is then obtained by directly injecting water in the glycerin-filled sample. As glycerin immediately and fully dissolves in water, thus losing its viscosity, the water full saturation is obtained by flushing two to three times the pore volume.

Processing method

Permeability measurement

To understand the fluid-flow effects at the sample scales, the rocks' transport properties have to be measured. The pressure gradient method (e.g., Ougier-Simonin et al., 2011) is used here (Appendix A). It consists in applying a pressure gradient and measuring the fluid flow. Knowing the pressure gradient and fluid flow allows one to measure the hydraulic conductivity across the sample, which is obtained for each confining step. Permeability is then directly inferred using Darcy's law, taking the sample's dimensions and the fluid viscosity as input parameters.

Strains oscillations: mechanical (elastic) response

At a given effective pressure, the confining pressure is maintained constant (i.e., $\Delta P_c = 0$), and an oscillating axial stress is exerted on the sample (i.e., $\Delta\sigma_{ax} \neq 0$). This oscillating stress $\Delta\sigma_{ax}$ leads to axial $\Delta\epsilon_{ax}$ and radial $\Delta\epsilon_{rad}$ strain oscillations (Figure 2a). Following the elastic theory for a homogeneous/isotropic cylindrical sample, LF Young modulus E_{LF} and Poisson ratio ν_{LF} may be inferred from such measurements (e.g., Batzle et al., 2006):

$$\Delta\epsilon_{ax} = \frac{1}{E_{LF}}\Delta\sigma_{ax} \quad \text{and} \quad \frac{\Delta\epsilon_{rad}}{\Delta\epsilon_{ax}} = -\nu_{LF}. \qquad (1)$$

For each frequency of applied $\Delta\sigma_{ax}$, axial and radial strains are recorded. A typical processing method is applied on the recorded signals (Pimienta et al., 2015), namely, (1) phase picking in Fourier domain (e.g., Batzle et al., 2006; Madonna and Tisato, 2013) to obtain the phase shift between the axial stress (i.e., end-platen's axial strain) and the sample's axial strain, which tangent is the attenuation on Young modulus Q_E^{-1}, (2) filtering in Fourier domain, and (3) linear regressions to obtain the relevant elastic moduli.

An example of strain oscillation is reported (Figure 2a) for the gypsum sample measured at a confining pressure of $P_c = 10$ MPa and axial added load of $\sigma^0_{ax} = 2$ MPa. The amplitude and frequency of the axial oscillation are here of $\Delta\sigma_{ax} \sim 0.2$ MPa (i.e., about $\Delta\epsilon_{alu} \sim 2.501^{-6}$) and $f = 0.1$ Hz, respectively, leading to sample's strains of about $\Delta\epsilon_{ax} \sim 4.501^{-6}$ and $\Delta\epsilon_{rad} \sim 1.501^{-6}$. The sample's Young modulus E_{LF} and Poisson ratio ν_{LF} are then obtained (Figure 2b) from a linear regression constrained with a 99% confidence interval. The data scatter around the linear regressions (i.e., E_{LF} and ν_{LF}) are used to infer a statistical error, noted respectively, ΔE_{LF} and $\Delta\nu_{LF}$. Note that, the applied strains on the sandstone samples of study are lower than approximately 10^{-5} to remain in the elastic domain.

Pore pressure oscillations: Hydraulic response

Following Pimienta et al. (2015), an additional information is obtained by measuring the fluid pressure oscillations at the outlet of the dead volume. Applying an oscillating deviatoric stress $\Delta\sigma_{ax}$ results in an oscillating pore fluid pressure (Figure 2c), which relates to the rock's compressibility and the fluid's diffusivity. The relevant parameter to understand a rock's hydraulic response in the case of an isotropic undrained loading is Skempton coefficient. In case of a deviatoric loading, the consolidation coefficient γ is the appropriate parameter (Wang, 2000). A pseudo-consolidation parameter γ^* is introduced here, defined as the ratio of pore fluid pressure at the dead volume outlet Δp_f to the deviatoric applied stress $\Delta\sigma_{ax}$ such that

$$\gamma^* = \frac{\Delta p_f}{\Delta\sigma_{ax}}. \qquad (2)$$

As for E_{LF} and ν_{LF} (Figure 2b), γ^* is obtained from a linear regression between Δp_f and $\Delta\sigma_{ax}$. An example of a LF (i.e., $f = 0.1$ Hz) stress oscillation inducing a pore pressure oscillation is reported (Figure 2c) for the water-saturated Fo7 sample. For this measure-

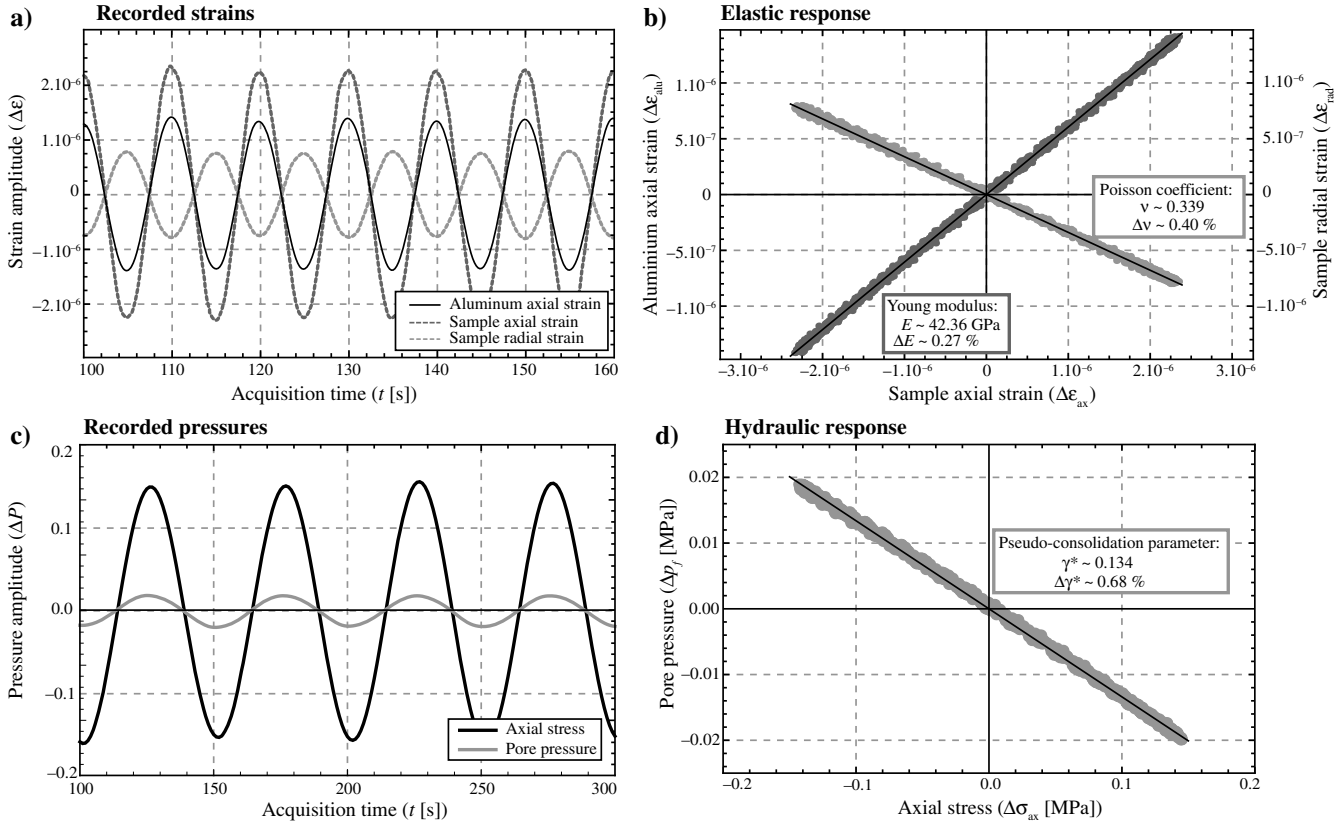

Figure 2. (a and b) Example of a standard measurement of Young's modulus E_{LF} and Poisson's ratio ν_{LF} for the gypsum sample for a confining pressure of 10 MPa and an axial stress of 2 MPa. (a) The oscillating aluminum's axial strain and the sample's axial and radial strains are recorded; and, knowing the aluminium Young modulus E_0, (b) linear regressions are calculated between the recorded strains to obtain E_{LF} and ν_{LF}. (c and d) Example of a measurement of the pseudo-consolidation parameter for Fo7 under water saturation at an effective pressure of 1 MPa and an axial stress of 0.2 MPa. (c) Oscillating stress (inferred from the recorded axial strain and E_0) and pore pressure are recorded and (d) the linear regression between both signals is calculated.

ment, the static conditions applied are an effective pressure of $P_{\text{eff}} = 1$ MPa (i.e., $P_c = 3$ MPa and $p_f = 2$ MPa) and an added deviatoric load of $\sigma^0_{\text{ax}} = 0.2$ MPa. The sample appears to be in a purely drained state so that an instantaneous response is observed on the pore pressure signal. As a direct consequence, the linear regression (Figure 2d) is almost a straight line. By increasing frequency, a phase shift between applied $\Delta\sigma_{\text{ax}}$ and induced Δp_f appears.

CALIBRATION RESULTS: MEASUREMENTS UNDER DRY CONDITIONS

The calibration is carried out following a stepwise procedure to assess the measuring accuracy of the apparatus. First, using the purely elastic glass and gypsum samples, the pressure and frequency dependence of the apparatus and procedure are tested. Then, in the particular case of the Plexiglas sample, the accuracy of the frequency dependence setup is tested. Finally, the role/effect of an added axial load on a rock's elastic response is tested using (1) the dependence to confining pressure of the dry Fontainebleau samples' elastic moduli for different values of axial load and (2) a comparison between bulk moduli obtained using the three different measuring setups (Figure 1).

Confining pressure effect for the reference samples

Measured Young's modulus and Poisson's ratio

Prior to measuring pressure-dependent rock samples, the pressure dependence of the axial setup needs to be assessed. The three standard samples are measured as a function of confining pressure (Figure 3) for given frequencies of $f \in [0.1, 1, 10, 100]$ Hz. To ascertain the measurement stability, an axial stress of about $\sigma^0_{\text{ax}} \sim 2$ MPa is applied for all measurements. The measurements are compared with the static values found in the literature for all three samples.

For the three samples, E_{LF} (Figure 3a) and ν_{LF} (Figure 3b) are independent of the confining pressure. The result is consistent with earlier K measurements on these nonporous standard samples (Pimienta et al., 2015). Furthermore, for all measuring frequencies in the range of $f \in [10^{-2} - 10^{2}]$ Hz, E_{LF} (Figure 3a) and ν_{LF} (Figure 3b) of the glass and gypsum samples fit and are in good agreement with the published static data. Note from the Plexiglas sample, that a frequency dependence is observed for all confining pressures. This effect is investigated in the "Inferred bulk modulus" section.

Inferred bulk modulus

In the framework of linear elasticity, under the assumption of an isotropic material, it is possible to infer the bulk modulus (i.e., K_{ax})

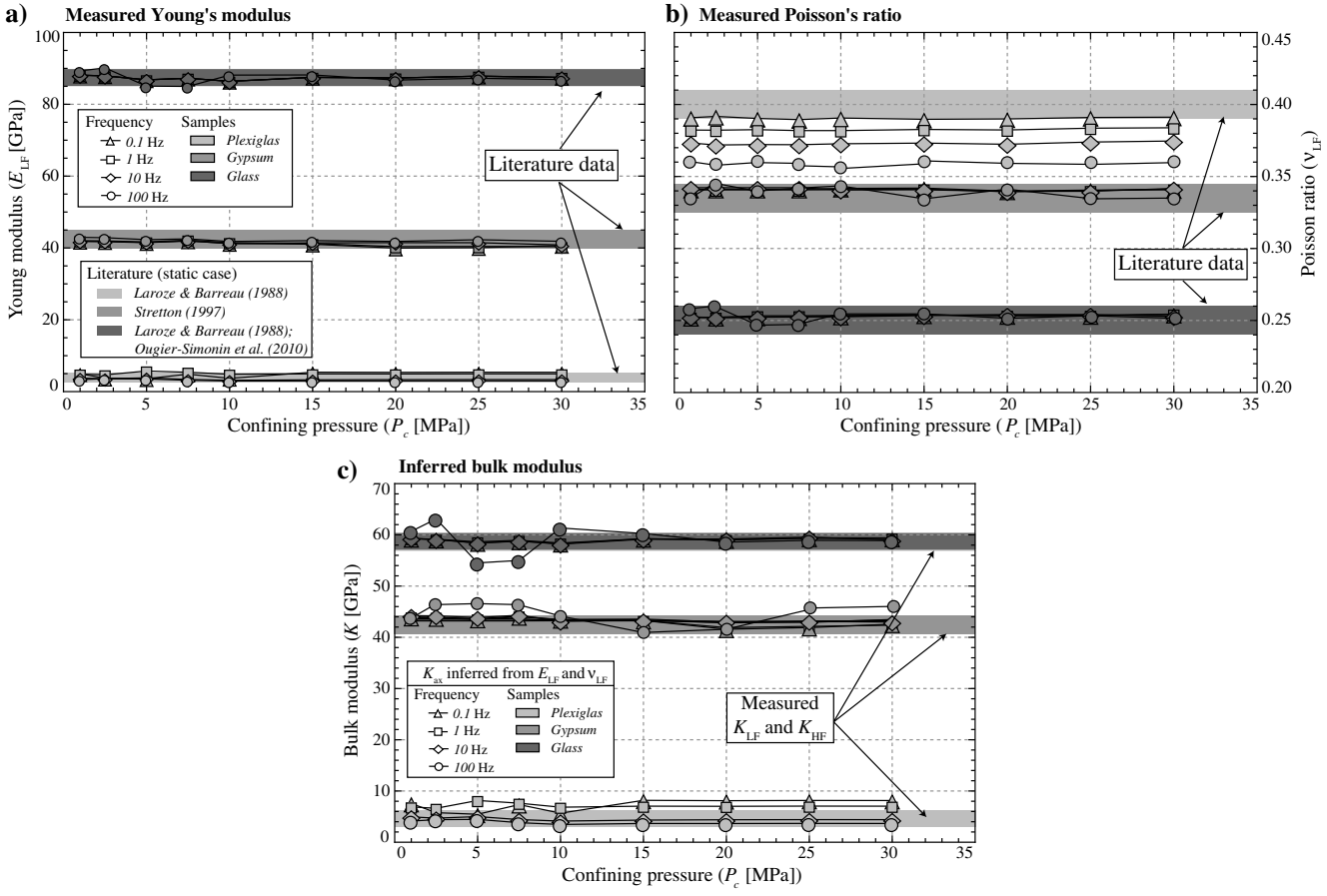

Figure 3. Measured pressure dependence of the elastic properties of the three reference samples from axial oscillations at four different oscillation frequencies of $f \in [0.1, 1, 10, 100]$ Hz. (a) Young's modulus E_{LF} and (b) Poisson's ratio ν_{LF} are directly measured for all confining pressures up to $P_c \sim 30$ MPa. (c) The standard samples' bulk modulus K_{ax}, inferred from E_{LF} and ν_{LF}, is compared with the K_{LF} and K_{HF} measured on the same samples (Pimienta et al., 2015).

by combining the measured E_{LF} and ν_{LF}. For all three samples, the pressure dependence of K_{LF} (Figure 1a) and K_{HF} (Figure 1b) have been measured in a previous study (Pimienta et al., 2015). For the three standard samples, the previously measured (i.e., K_{LF} and K_{HF}) and inferred from this work (i.e., K_{ax}) bulk moduli are compared as a function of pressure (Figure 3c).

For the three standard samples, K_{ax} fits with measurements using the different measuring setups (Figure 1) for all confining pressures (Figure 3c). It thus indicates the reproducibility of the measurements using the different setups.

Frequency effect for the Plexiglas sample

The frequency dependence of the Plexiglas sample is further investigated to test the accuracy of the apparatus. The Young's modulus E_{LF}, Young's attenuation Q_E^{-1}, and Poisson's ratio ν_{LF} are measured as a function of frequency in the range $f \in [10^{-2}; 10^{2}]$ Hz that is allowed by the apparatus. Although the frequency dependence of this material is known to vary from sample to sample (e.g., Madonna and Tisato, 2013), the measurements are compared with the existing data (Batzle et al., 2006; Madonna et al., 2011; Tisato and Madonna, 2012) on Plexiglas samples.

Attenuation of the Plexiglas Young's modulus

To the authors' knowledge, Young's attenuation Q_E^{-1} is the Plexiglas elastic property that was the most measured (Batzle et al., 2006; Madonna et al., 2011; Tisato and Madonna, 2012). The frequency-dependent measurements of this property, compared with the existing data sets, are thus reported first (Figure 4). The measured Q_E^{-1} shows values ranging between 0.04 and 0.08 over the frequency range of study.

A large attenuation peak, of about $Q_E^{-1} = 0.08$, is observed from the measurements at $f = 15$ Hz. Comparing the present Q_E^{-1} data to reported data (Figure 4), very similar behaviors are observed. Data reported by Madonna et al. (2011) and Tisato and Madonna (2012) show a similar peak at approximately 0.08 and the same frequency of approximately 15 Hz. For the different temperatures (i.e., 23°C and 40°C) of measurement, the Q_E^{-1} peaks measured by Batzle et al. (2006) are slightly higher (i.e., 0.09 and 0.1) and at higher frequencies (i.e., approximately 50 and 100 Hz). It indicates that the Plexiglas investigated here and that of Madonna et al. (2011) and Tisato and Madonna (2012) are very similar and were measured under very similar in situ conditions. Comparison with Batzle et al. (2006) results shows that the Plexiglas they use and/or the in situ measuring conditions are slightly different. As shown by Batzle et al. (2006), the Q_E^{-1} peak is shifted to higher magnitudes and higher frequencies as the temperature increases. The temperature during the present measurements was of about $T = 20$°C, which could explain the lower magnitude in the Q_E^{-1} peak measured.

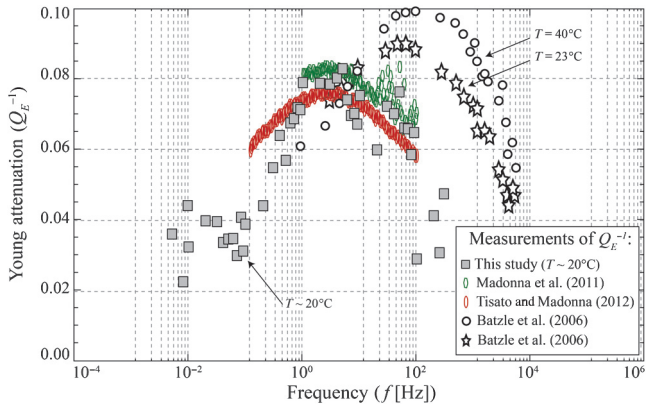

Figure 4. Measured frequency dependence of Young attenuation Q_E^{-1} of the Plexiglas sample for a confining pressure of 10 MPa and an axial stress of 2 MPa. Existing LF measurements of Q_E^{-1} found in the literature (Batzle et al., 2006; Madonna et al., 2011; Tisato and Madonna, 2012) are reported for comparison.

Finally, a small peak of $Q_E^{-1} \sim 0.04$ (Figure 4) appears at lower frequencies (i.e., $f \in [5.10^{-3}; 10^{-1}]$ Hz). Studies from the literature do not report measurements at frequencies lower than $f = 10^{-1}$ Hz, so that no comparison can be made for this second peak. Note however that this second frequency-dependent variation correlates with the K_{LF} and Q_K^{-1} variations measured in the same frequency range (i.e., $f \in [510^{-3}; 510^{-1}]$ Hz) for this Plexiglas sample (Pimienta et al., 2015).

Elastic dispersion on the Plexiglas sample

Frequency dependent E_{LF} (Figure 5a) and ν_{LF} (Figure 5b) are reported for the Plexiglas sample. To understand the frequency-dependent variations, the measurements are compared with limit cases of (1) HF measurements (i.e., E_{HF} and ν_{HF}) and (2) the static values found in the literature (e.g., Boudet and Ciliberto, 1998). In case of the frequency-dependent E_{LF}, an existing data set is found in the literature that is also reported for comparison (Batzle et al., 2006).

A large frequency-dependent increase is observed on E_{LF} (Figure 5a) that correlates with the measured Q_E^{-1} (Figure 4). Comparing to the end values reported shows an overall consistency. The E_{LF} at very LF is close to the static value from the literature (Boudet and Ciliberto, 1998). It increases with increasing frequency, up to a value at $f = 10^2$ Hz close to that from ultrasonic measurement E_{HF}. This may indicate that no dispersion effect is expected in this sample at higher frequencies. As for Q_E^{-1} (Figure 4), E_{LF} differs slightly from the one measured by Batzle et al. (2006) that keeps on increasing at frequencies higher than about $f = 10^2$ Hz. The difference is to be related to the difference in the Plexiglas used and/or the measuring conditions (e.g., temperature). Note finally that a slope change is observed at about $f = 10^{-1}$ Hz, which correlates with the behavior of Q_E^{-1} (Figure 4).

In case of frequency-dependent Poisson ratio ν_{LF}, the authors do not know of any existing measurement for Plexiglas. The measurements are thus only compared to the HF measurements and to the published static value (e.g., Boudet and Ciliberto, 1998). Overall, ν_{LF} (Figure 5b) shows a continuous decrease with increasing frequency. At LF (i.e., $f \sim 10^{-2}$ Hz), it is close to the static value of $\nu_{stat} \sim 0.4$ (Boudet and Ciliberto, 1998). As the frequency increases, it progressively decreases down to a value at $f \sim 10^2$ Hz close to the one inferred from ultrasonic velocities of $\nu_{HF} \sim 0.36$. Consistently with the measured E_{LF} (Figure 5a), no dispersion is thus expected in the frequency band of $f \in [10^2; 10^6]$ Hz for this sample.

Effect of the static axial load on dry rock samples

As introduced earlier, the reported standard samples' properties were measured under a small deviatoric load of about $\sigma_{ax}^0 = 2$ MPa.

A small axial load is indeed needed (e.g., Subramaniyan et al., 2014) to (1) ascertain parallelism and (2) provide stable measurements. Because the standard samples are neither porous nor microcracked, this deviatoric load does not affect the sample's internal microstructure. However, sedimentary rocks contain microcracks that are sensitive to pressure. In that case, what is the effect of this σ^0_{ax}?

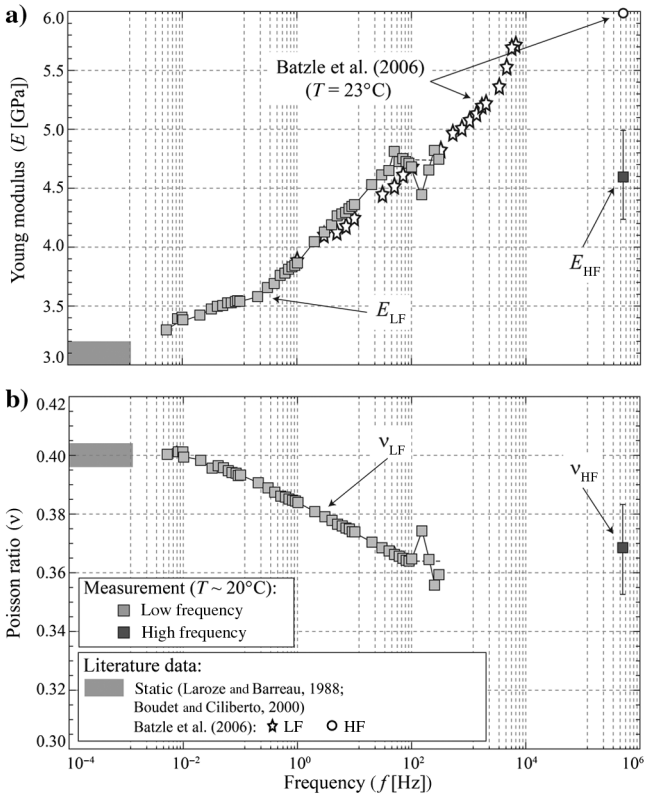

Figure 5. Measured frequency dependence of the (a) Young modulus E_{LF} and (b) Poisson ratio ν_{LF} of the Plexiglas sample for a confining pressure of 10 MPa and an axial stress of 2 MPa. The HF measurements and static data from the literature are reported. In addition, existing data on E_{LF} and E_{HF} (Batzle et al., 2006) are reported for comparison.

Change in overall behaviors with static axial load

The pressure dependence of E_{LF} and ν_{LF} is reported (Figure 6) for the dry Fo7 for three different axial loads of $\sigma^0_{ax} = [0.2; 2.2; 6.5]$ MPa. Consistently, no frequency dependence is measured under dry conditions, and a dependence to confining pressure is observed. It appears that a small deviatoric load (i.e., $\sigma^0_{ax} < 6.5$ MPa) strongly affects the resulting sample's elastic properties for confining pressures lower than approximately 10 MPa. For E_{LF} (Figure 6a) and ν_{LF} (Figure 6b), three distinct pressure-dependent curves are observed. At low confining pressures (i.e., $P_c < 10$ MPa), E_{LF} appears to increase for an increasing value of σ^0_{ax}. Interestingly, σ^0_{ax} induces a clear change in ν_{LF} (Figure 6b) pressure dependency.

This shift in pressure dependencies measured on ν_{LF} can be explained by a change in the rock's overall isotropic properties. Following Wang et al. (2012), the measured dry V_P/V_S ratio (i.e., ν) is expected to increase with increasing P_c for isotropic rocks. However, it could decrease with increasing P_c for an anisotropic rocks if measured in the appropriate orientation. The rock is initially isotropic. The axial pressure σ^0_{ax} closes the horizontal small aspect ratio microcracks, thus inducing an anisotropy.

Testing the sample's isotropy

To check the isotropy using the present measuring setup, it is possible to compare the measurements to the ones measured under zero deviatoric stress. For that purpose, one can use K_{LF} and K_{HF}, measured under pure isotropic conditions (Figure 1a and 1b). For dry Fo7 (Figure 7a) and Fo8 (Figure 7b) samples, E_{LF} and ν_{LF} have been measured under the lowest added axial load (i.e., $\sigma^0_{ax} = 0.2$ MPa). The inferred K_{ax} is compared with K_{LF} and K_{HF} measured on the same Fontainebleau samples (Pimienta et al., 2015).

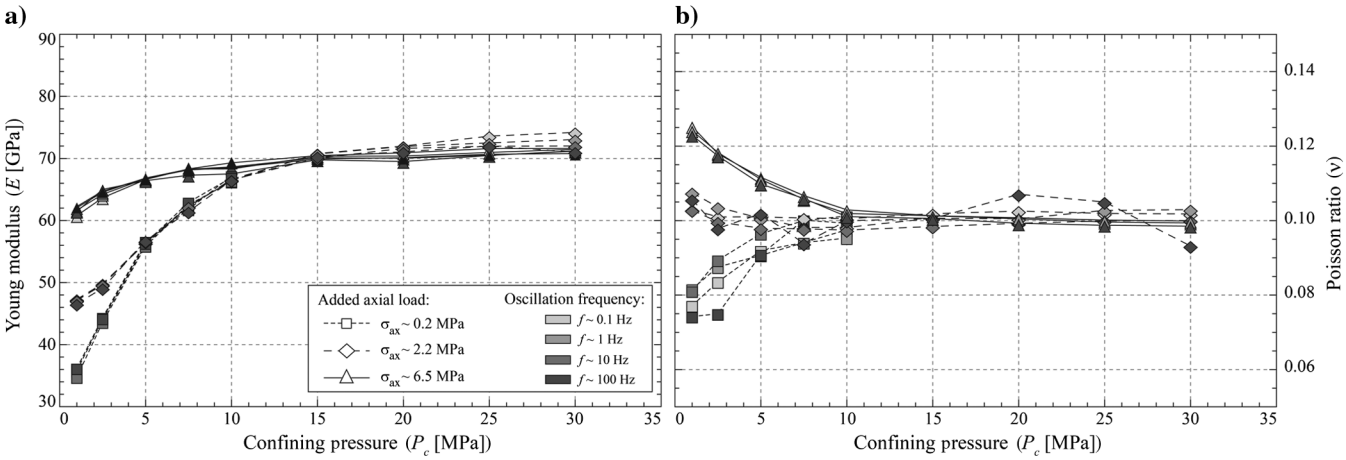

Figure 6. Measured pressure dependence of the (a) Young modulus E_{LF} and (b) Poisson ratio ν_{LF} of the dry Fo7 for different values of axial load σ^0_{ax}. Four different oscillation frequencies (i.e., symbols) of $f \in [0.1, 1, 10, 100]$ Hz are chosen.

At all confining pressures, K_{ax} falls in the uncertainty range of measured K_{LF} and K_{HF}. It implies that this added axial load is low enough, and that no stress-induced anisotropy effect is visible. As a consequence, we choose to fix this static axial load in the following at $\sigma^0_{ax} = 0.2$ MPa.

EFFECT OF FLUIDS ON SANDSTONE SAMPLES' YOUNG MODULUS

The frequency and pressure dependence of the three main parameters have been investigated in both sandstone samples: (1) Young's modulus E_{LF}, (2) Young's attenuation $Q_E{}^{-1}$, and (3) pseudo-consolidation parameter γ^*.

Pressure dependence of the samples' Young's modulus

For Fo8 (Figure 8a and 8b) and Fo7 (Figure 8c and 8d), the pressure dependence of E_{LF} has been investigated in case of the glycerin- and water-saturated samples for four measuring frequencies of $f = [0.1; 1; 10; 100]$ Hz. The dry E_{LF} is reported for comparison. The values of E_{HF} measured under fluid-saturated conditions are also reported for comparison in case of Fo7. Overall, the pressure dependence is very strong for Fo7 and weak for Fo8. Under fluid saturation, increasing the frequency leads to a large decrease in this pressure dependence for both rocks. At effective pressures beyond approximately 10 MPa, the measurements are only slightly higher than the dry E_{LF} for all frequencies.

The Fo8 sample (Figure 8a and 8b) shows no measurable pressure dependence under fluid-saturated conditions for frequencies higher than about $f = 10$ Hz. Almost no difference between glycerin and water saturation is measured. Fo7 shows much larger effects. A clear distinction between fluid, pressure and frequency effects is observed. At confining pressures below 10 MPa, the fluid-saturated Young modulus increases with frequency, up to the measured E_{HF}. For any frequency, the glycerin-saturated Young modulus results higher than the water-saturated one.

Frequency dependence of Young modulus for Fo7 sample

The frequency dependence of Young's modulus E_{LF} and attenuation $Q_E{}^{-1}$, measured on Fo7 saturated by either water (Figure 9a and 9c) or glycerin (Figure 9b and 9d), is reported for five different effective pressures up to $P_{eff} = 30$ MPa. A large effect of frequency is measured on E_{LF} (Figure 9a and 9b) that varies with the fluid and pressure. For a given P_{eff}, the increase of E_{LF} occurs at higher frequency and is of lower magnitude for the water-saturated case as compared with the glycerin one.

Furthermore, for both saturated cases, P_{eff} appears to damp the frequency dependence of E_{LF} and $Q_E{}^{-1}$. In particular, at $P_{eff} \sim 30$ MPa, no frequency dependence is measured on water and glycerin saturated E_{LF} and $Q_E{}^{-1}$. On the reverse, at the lowest P_{eff} conditions (i.e., $P_{eff} = [1; 2.5]$ MPa) a large increase with frequency is observed. In the particular case of the glycerin-saturated sample at 1 MPa, E_{LF} increases from 38 to approximately 60 GPa. A large $Q_E{}^{-1}$ peak is associated with that increase. The $Q_E{}^{-1}$ peak has a maximum of 0.12 at about $f \sim 1$ Hz. The same observations are made at a P_{eff} of 2.5 MPa.

Frequency dependence of hydraulic properties

As introduced earlier, the stress-induced pore pressure oscillations in the dead volume are described through a pseudo-consolidation parameter γ^*. The frequency dependence of this property is investigated for Fo7 saturated by either water (Figure 10a) or glycerin (Figure 10b). The different effective pressures of $P_{eff} = [1; 2.5; 5; 10; 30]$ MPa are investigated.

Here, γ^* decreases with increasing effective pressure at lowest frequencies. Furthermore, for a given effective pressure, γ^* decreases when frequency increases in water- and glycerin-saturated conditions. The glycerin case (Figure 10b) shows a monotonic decrease down to $\gamma^* = 0$ at about $f = 1$ Hz. On the reverse, the water-saturated case (Figure 10a) shows a sharp decrease between 0.2 and 2–20 Hz.

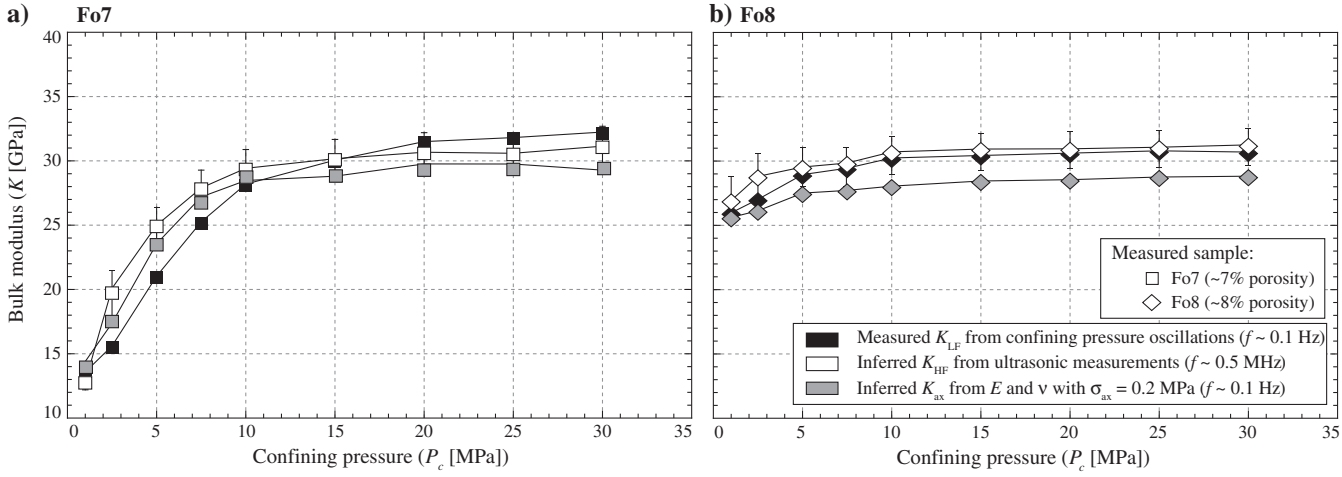

Figure 7. Pressure dependence for the dry (a) Fo7 and (b) Fo8 samples of the bulk modulus measured using the different experimental setups (Figure 1). The K_{ax}, inferred from E_{LF} and ν_{LF} (Figure 1c) at the lowest axial load (i.e., $\sigma^0_{ax} = 0.2$ MPa), is compared with the K_{LF} (Figure 1a) and K_{HF} (Figure 1b) measured under purely isotropic conditions (Pimienta et al., 2015).

The frequency-dependent decrease of γ^* corresponds to a decreasing fluid flow out of the sample (Pimienta et al., 2015). Under water- and glycerin-saturated conditions, a frequency can be reached for which no flow out of the sample can be observed. In agreement with measurements of E_{LF} (Figure 9a), the frequency of the observed decrease in fluid flow γ^* occurs at much lower frequencies in case of the glycerin saturation.

INTERPRETATION AND DISCUSSION

Large frequency-dependent variations in Young's modulus and attenuation are measured that depend on the saturating fluid. In addition, the variations in γ^* indicate the existence of frequency-dependent fluid flow, which also depend on the saturating fluid. First, the role of the fluid's viscosity in these frequency-dependent variations is questioned and accounted for. Then, the measurements are interpreted in terms of fluid flow at different scales. Finally, the frequency-dependent E_{LF} and Q_E^{-1} measured on Fo7 are compared with the reported measurements of bulk modulus dispersion and attenuation on the same rock (Pimienta et al., 2015).

Viscosity effect and apparent frequency

In the framework of the fluid flow theories, apparent frequency f^* that accounts for fluid's viscosity η_f and frequency f in the same manner is a key parameter. It is defined as

$$f_f^* = f.\frac{\eta_f}{\eta_0}, \tag{3}$$

with $\eta_0 = 10^{-3}$ Pa.s and η_f the fluid's viscosity.

Assessment of fluids' in situ viscosity

From the measured hydraulic conductivities (Appendix A), about two to three orders of magnitudes separate the water- from the glycerin-saturated measurements. If one assumes the permeability values to be identical for both fluids, the difference between fluids' in situ viscosities does not correspond to the theoretical ratio (i.e., $\eta_{wat}/\eta_{gly} \sim 1221$) but to the ratio $\eta_{wat}/\eta_{gly} \sim 350$.

The in situ water viscosity is assumed to be $\eta_{wat} = \eta_0$. The resulting in situ glycerin's viscosity is thus of $\eta_{gly} = 350\eta_0$. The values of in situ viscosities being assessed for each fluid η_f, the apparent frequency f^* can be obtained. Considering the range of

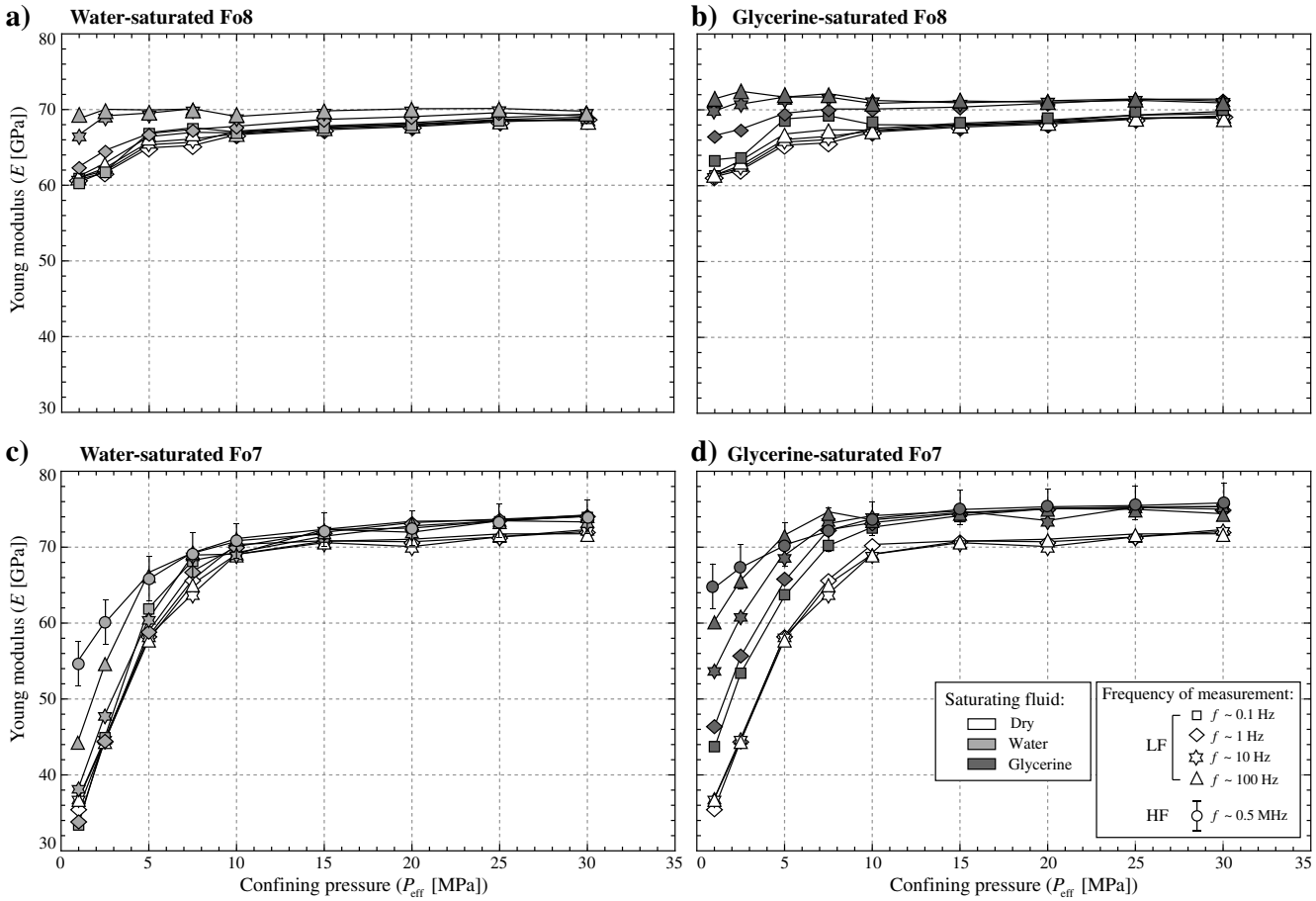

Figure 8. Measured pressure dependence of the Young modulus E_{LF} of the dry and fluid saturated (a and b) Fo8 and (c and d) Fo7. Four different oscillation frequencies (i.e., symbols) of $f = [0.1; 1; 10; 100]$ Hz are chosen for the E_{LF} measurement. The fluid-saturated E_{HF} is also reported for Fo7 sample.

frequencies measured of $f \in [510^{-3}; 10^{2}]$ Hz, the apparent frequency range (1) for water saturation (i.e., $\eta_{wat} = 10^{-3}$ Pa.s) is of $f^{*}_{wat} \in [510^{-3}; 10^{2}]$ Hz and (2) for glycerin saturation (i.e., $\eta_{gly} = 0.35$ Pa.s) is of $f^{*}_{gly} \in [1.75; 0.3510^{5}]$ Hz.

Young's modulus variations with apparent frequency

The Young's modulus and attenuation are plotted as a function of apparent frequency (Figure 11) for different effective pressures of $P_{eff} = [1; 2.5; 5; 10]$ MPa. No variations are observed for

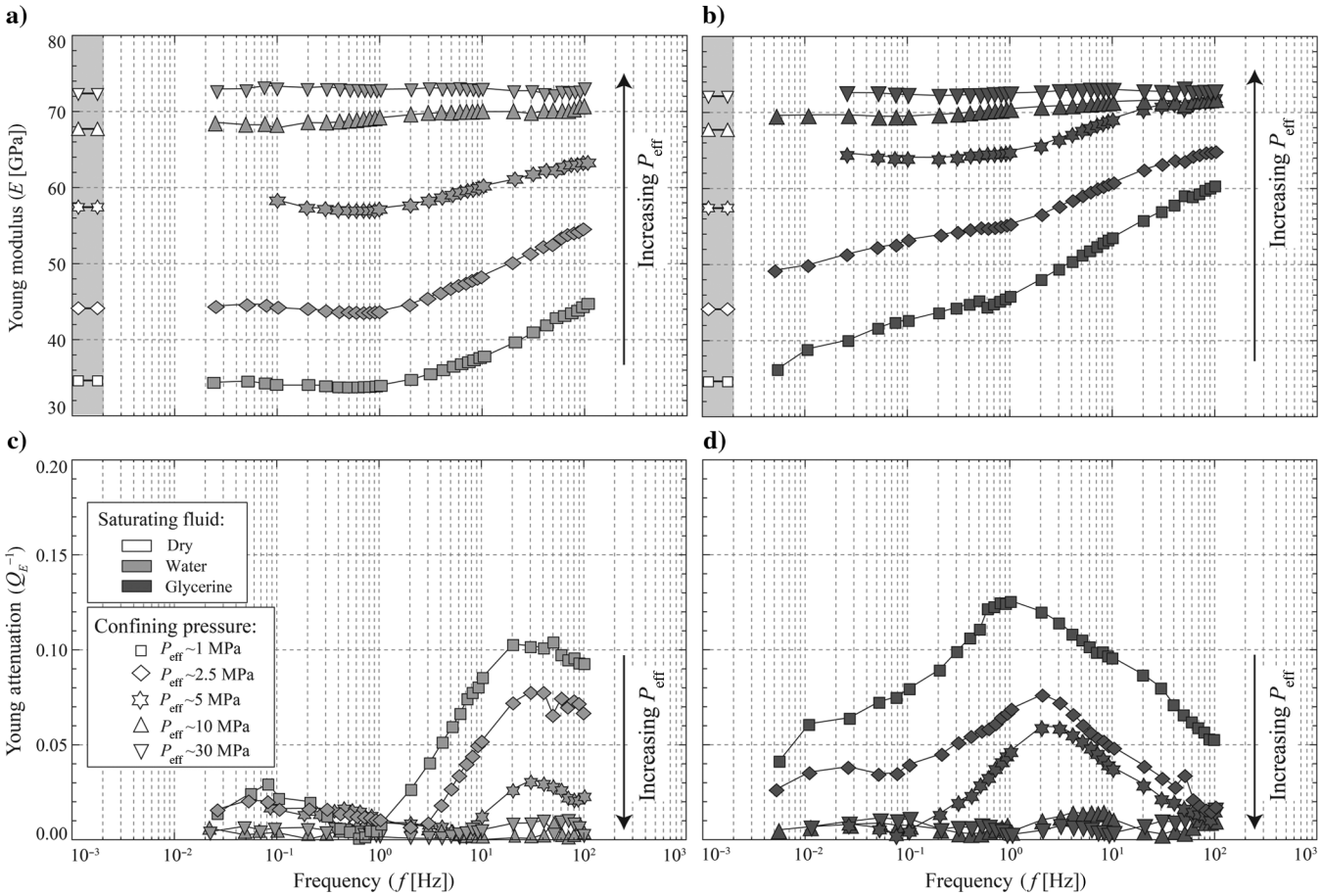

Figure 9. Measured frequency dependence of the Young (a and b) modulus E_{LF} and (c and d) attenuation $Q_E{}^{-1}$ of Fo7 fully saturated by water or glycerin at different confining pressures.

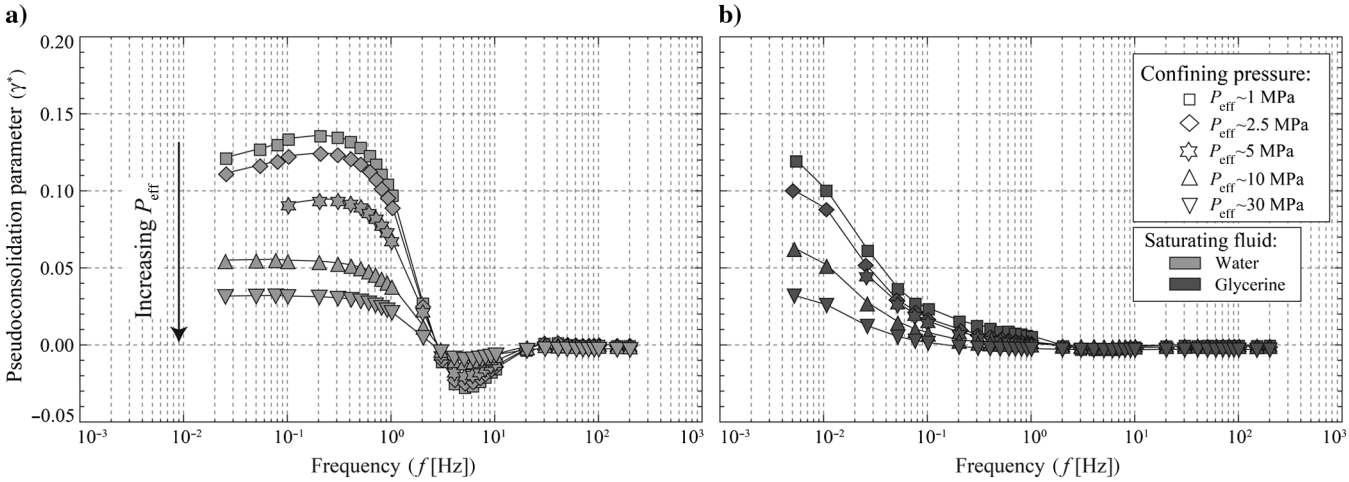

Figure 10. Measured frequency dependence of the pseudo-consolidation parameter for Fo7 fully saturated by (a) water or (b) glycerin at different confining pressures.

$P_{\text{eff}} = 30$ MPa so that this case is not considered here. The frequencies allowed by the apparatus lead to measurements over the apparent frequency range of $f^* \in [10^{-3}; 10^5]$ Hz. Furthermore, there is an overlap for a few measurements under different saturation conditions.

Overall, a good fit is obtained between measurements of Young moduli (Figure 11a) under either water or glycerin saturation. At low effective pressure $P_{\text{eff}} \in [1; 2.5; 5]$ MPa, a progressive increase in modulus is measured with increasing apparent frequency. At lowest effective pressure, this increase is as large as approximately 30 GPa over the range of apparent frequencies. For all effective pressures, the increase in E_{LF} with apparent frequency shows a slope change at a frequency of 100 Hz. In addition, ${Q_E}^{-1}$ (Figure 11b) presents a large peak for f^* close to 10^2 Hz. The peak shows the same magnitude for water- and glycerin-saturated cases, but it occurs at slightly higher f^* for the glycerin-saturated case. At $P_{\text{eff}} = 10$ MPa and beyond, very little variations are measured on E_{LF} and ${Q_E}^{-1}$.

In the low P_{eff} range and for $f^* \in [1; 50]$ Hz, $E_{\text{gly}} > E_{\text{wat}}$. This could be related to the fluids' intrinsic bulk modulus, which is higher for glycerin (i.e., 4.4 GPa) than for water (i.e., 2.2 GPa).

Fluid flow at different scales in Fo7

As reported in Pimienta et al. (2015), the drained/undrained and undrained/unrelaxed transitions are expected in the investigated frequency range (i.e., $f^* \in [10^{-3}; 10^5]$ Hz) for the Fo7 sample. How well do the present results fit with this previous interpretation?

Observed transitions between regimes

We consider here a REV of the rock sample. This volume corresponds to a scale that is much larger than the pores or grains, large enough to observe an approximately homogeneous volume, and much lower than the sample's scale. In the drained regime, fluid has time to flow in and out of the REV, so that this case corresponds to the dry one. Measurements under water-saturated conditions at frequencies lower than $f^* = 1$ Hz (Figure 11a) prove to correspond to such regime. In the undrained regime, the fluid mass is constant within the REV, and the K_{ud} results are higher than the drained K_d. The data from Pimienta et al. (2015) fit to the drained/undrained transition in the range of $f^* \in [1; 10^2]$ Hz, the undrained K_{ud} being reached at frequencies below $f^* = 10^2$ Hz. This same transition could explain the increase of E_{LF} observed at frequencies below $f^* = 10^2$ Hz (Figure 11a). Furthermore, a small plateau might be observed at about $f^* = 10^2$ Hz, which could indicate an undrained regime. If, in agreement with poroelasticity, the shear modulus is constant (i.e., $G_{\text{ud}} = G_d$), it is indeed expected that E_{ud} should be higher than E_d. The observed variations are consistent with the predicted cut-off frequency for this transition, expected to take place at $f_1^* = 10$ Hz (Pimienta et al., 2015).

In the unrelaxed regime, fluid has no time to flow from one inclusion (i.e., pore or crack) to the neighboring one, and the REV is not isobaric. The relaxed/unrelaxed transition is expected to take place at higher frequency than the drained/undrained one, and to result in larger elastic moduli. This second transition could explain the increase in E_{LF} starting from the plateau at $f^* = 10^2$ Hz up to the large E_{HF} value (Figure 11a). This interpretation is consistent with the predicted cut-off frequency for this second transition that is expected to take place at $f_2^* = 10^3$ Hz (Pimienta et al., 2015).

One may thus consider that the data for E_{LF} variations (Figure 11a) could be related to the (1) drained to undrained transition in the range of $f^* \in [10^0; 10^2]$ Hz and (2) relaxed to unrelaxed transition in the range of $f^* \in [10^2; 10^5]$ Hz. Then, the attenuation data are expected to show two distinct attenuation peaks at the frequencies of f_1^* and f_2^*, respectively. This is not the case (Figure 11b). A possible explanation is that the two transitions are too close, so that the two attenuation peaks overlap. The pressure has a strong effect on these two transitions, so that at $P_{\text{eff}} = 10$ MPa and beyond, no variation is observed.

Dispersion and attenuation in terms of the Zener model

From the general theory of linear viscoelastic response and Kramers-Kronig relations (e.g., Nowick and Berry, 1972), dispersion and attenuation phenomena correlate. The measured frequency-dependent variations can be investigated using the Zener model. This simple viscoelastic model uses a combination of a

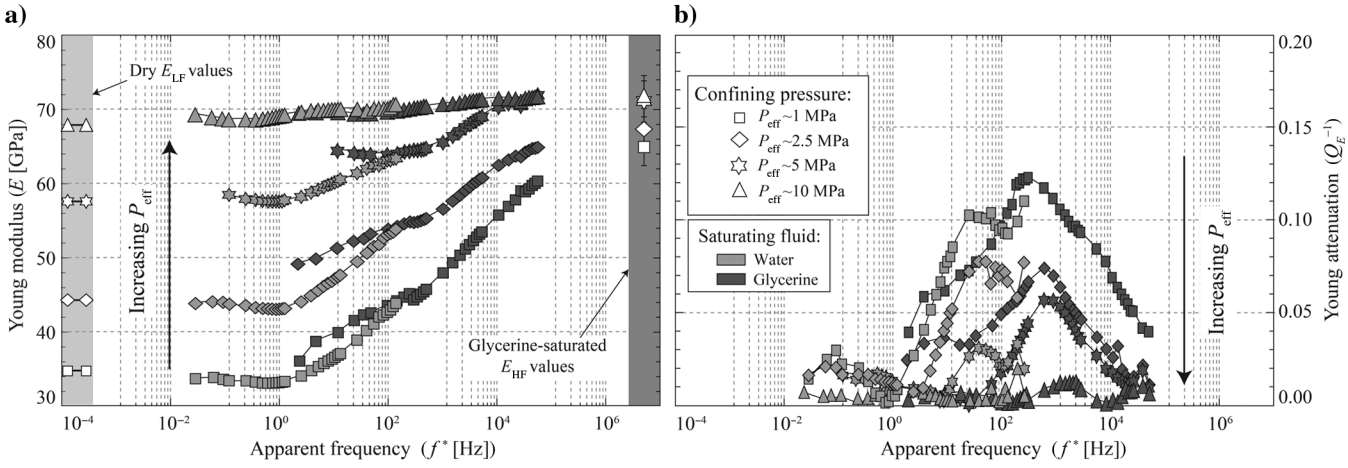

Figure 11. Measured dependence to apparent frequency of the (a) Young's modulus E_{LF} and (b) Young's attenuation ${Q_E}^{-1}$ of the fully saturated Fo7. The water and glycerin viscosities, allowing to fix the apparent frequency, are, respectively, of $\eta_{\text{wat}} = 10^{-3}$ Pa.s and $\eta_{\text{gly}} = 0.35$ Pa.s. Different effective pressures of $P_{\text{eff}} = [1; 2.5; 5; 10]$ MPa are reported. Dry E_{LF} and glycerin-saturated E_{HF} values are reported for comparison.

spring (of stiffness/modulus M_a) in series with a parallel assemblage of a spring (of stiffness/modulus M_b) and a dashpot (of viscosity η_b). Noting that $M_0^{-1} = M_a^{-1} + M_b^{-1}$ and $\tau_0 = \eta_b(M_a + M_b)^{-1}$, it can be shown that the complex modulus $\bar{M}(\omega)$ takes the form

$$\bar{M}(\omega) = \frac{M_0 + i\omega\tau_0 M_a}{1 + +i\omega\tau_0}, \tag{4}$$

where $\omega = 2\pi f$ is the pulsation and τ_0 is the characteristic relaxation time. Noting that $\bar{M}(\omega) = M_R(\omega) + iM_I(\omega)$, one determines the magnitude $M(\omega) = \sqrt{M_R^2 + M_I^2}$ and attenuation $Q^{-1}(\omega) = M_I/M_R$.

This model relies on three parameters (i.e., M_a, M_b, and η_b). From limit considerations, M_a and M_0 are obtained, respectively, at the highest and the lowest frequencies of the transition of interest. Furthermore, η_b may be obtained from the knowledge on the characteristic relaxation time τ_0 (or critical frequency f_c) of the effect. The fit to a Zener model allows us to calculate the dispersion/attenuation curves expected in the case of drained/undrained or relaxed/unrelaxed transitions if the elastic properties of the three regimes are known. For these two transitions, the two critical frequencies f_c chosen are assumed to be 10^1 Hz (i.e., f_1^*) and 10^3 Hz (i.e., f_2^*).

We apply the Zener model (equation 4) to our data using for E_{ud} either the measured value at 10^2 Hz (i.e., E_{ud}^{meas}) or that predicted from the Biot-Gassmann equation (i.e., E_{ud}^{th}). Note that, for each prediction, we use two sets of parameters because we have two transitions. We assume that the drained (i.e., E_d) and unrelaxed (i.e., E_{ur}) Young moduli are known. They are obtained from the data, i.e., $E_d = E_{dry}$ and $E_{ur} = E_{HF}$. We calculate for E and Q_E^{-1} two sets of distinct curves depending on the choice of E_{ud}. The first one, using only the data, corresponds to a transition from E_d to E_{ud}^{meas} (i.e., drained/undrained) and from E_{ud}^{meas} to E_{ur} (i.e., relaxed/unrelaxed). The second one, using Biot-Gassmann prediction, corresponds to a transition from E_d to E_{ud}^{th} (i.e., drained/undrained) and from E_{ud}^{th} to E_{ur} (i.e., relaxed/unrelaxed). The two dispersion and attenuation curves are compared with the data set (Figure 12) for two effective pressures of $P_{eff} = [1; 2.5]$ MPa. The Biot-Gassmann prediction of the undrained Young modulus is shown for comparison.

In case of the Young's modulus dispersion (Figure 12a and 12b), the measurements at 1 and 2.5 MPa show the same overall behaviors and lead to the same interpretations. The Zener plot using

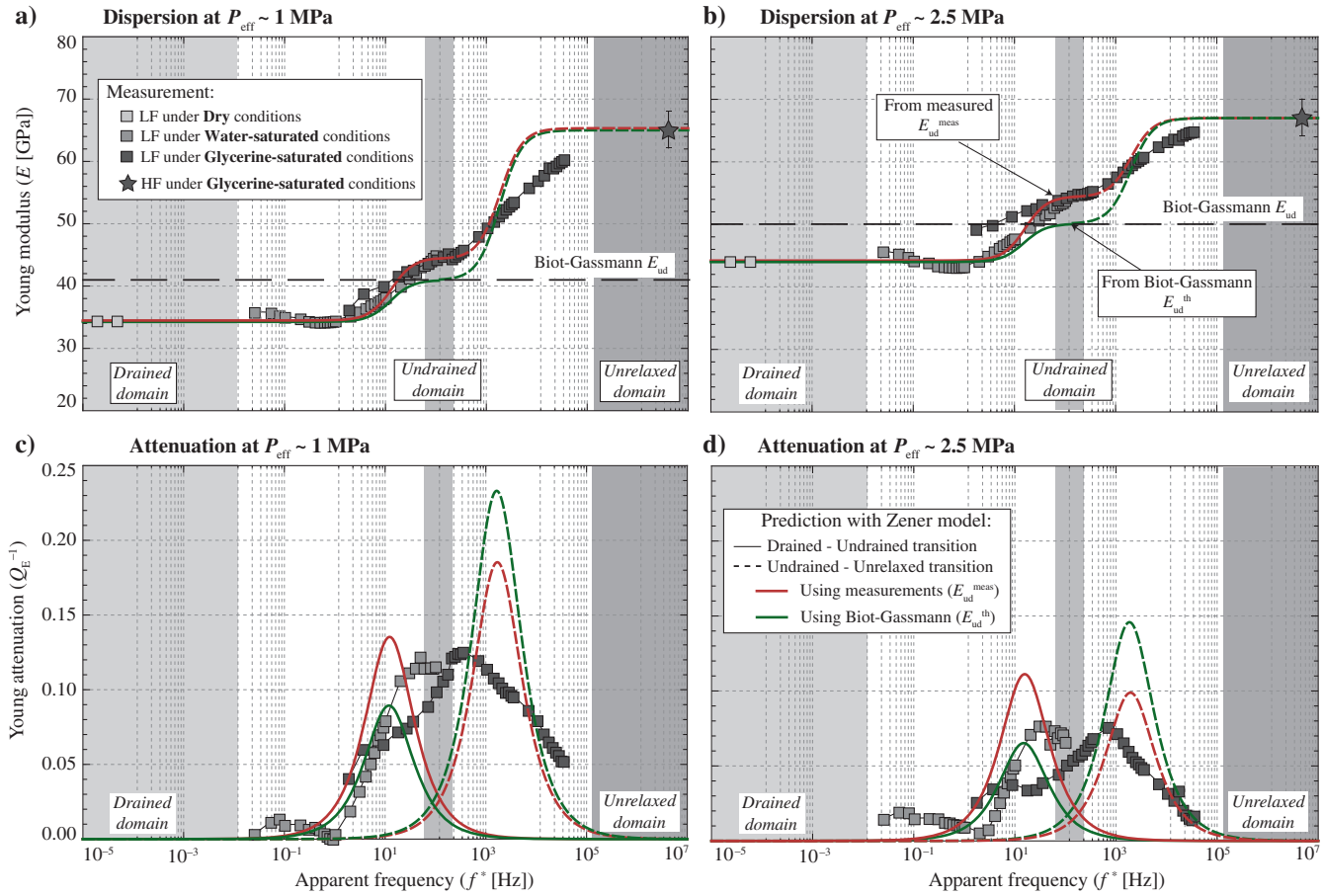

Figure 12. Measured (a and b) Young modulus and (c and d) attenuation of the fluid-saturated Fo7 as a function of f^* for $P_{eff} = [1; 2.5]$ MPa. Measurements are compared with the Zener-like variations expected for the drained/undrained (i.e., filled curve) and relaxed/unrelaxed (i.e., dashed curve) transition. The two sets of curves are predicted using the measured E_{ud}^{meas} (i.e., red) and predicted E_{ud}^{th} (i.e., green) undrained Young modulus.

Biot-Gassmann prediction is slightly below the Zener plot using the data for the drained/undrained transition. The Zener plot using E_{ud}^{meas} fits the data frequency dependence for the drained/undrained transition, but it deviates from it in the case of an undrained/unrelaxed transition. For all $f^* > 10^2$ Hz, the plot overestimates the measurements, indicating that the measured dispersion is more spread out than expected in the case of an unique frequency effect. This spreading may be explained by a distribution in microcracks of differing aspect ratio inside this natural rock.

The measured Q_E^{-1} (Figure 12c and 12d) shows a peak similar in amplitude to the ones predicted by the Zener plots in the case of the drained/undrained transition. For the relaxed/unrelaxed transition, both Zener plots overestimate the peak.

Young's modulus and bulk modulus variations

The bulk modulus K_{LF} and attenuation Q_K^{-1} were measured on the same sample (Pimienta et al., 2015). The two data sets are reported (Figure 13a and 13b). As in the previous section, the measurements are plotted as a function of apparent frequency and compared with two Zener plots. Again, the drained regime (i.e., K_d and E_d) and the unrelaxed regime (i.e., K_{ur} and E_{ur}) are directly measured. The sole difference between the two Zener plots is in the choice for the value of the undrained regime. The first Zener plot is obtained using the measured undrained modulus (i.e., E_{ud}^{meas} and K_{ud}^{meas}). The second Zener plot is obtained using Biot-Gassmann prediction (i.e., E_{ud}^{th} and K_{ud}^{th}).

Dispersion in elastic moduli

Assuming linear isotropic elasticity, it is possible to infer from E and K the Poisson ratio ν and the shear modulus G. Because the bulk and Young modulus data sets do not cover the same frequency range, ν and G are inferred using the calculated Zener plots (Figure 13c and 13d). Measured data on dry ν_d and glycerin-saturated ν_{HF} and G_{HF} are reported, along with G_d inferred from the measured ν_d and E_d. For ν and G, an increase is observed between the dry LF and glycerin-saturated HF data. Yet, the two elastic properties show different behaviors at intermediate frequencies.

For the shear modulus (Figure 13d), both Zener plots show a monotonic increase with frequency. Using Biot-Gassmann theory (i.e., E_{ud}^{th} and K_{ud}^{th}), no change in G for the drained/undrained transition is predicted. The small variation observed corresponds to a numerical artifact from combining K and E Zener plots. The G dispersion is expected to occur during the relaxed/unrelaxed transition. Using the direct data fit (i.e., E_{ud}^{meas} and K_{ud}^{meas}), a slight increase of G is however predicted for the drained/undrained transition such that $G_{ud} > G_d$. The relaxed/unrelaxed transition

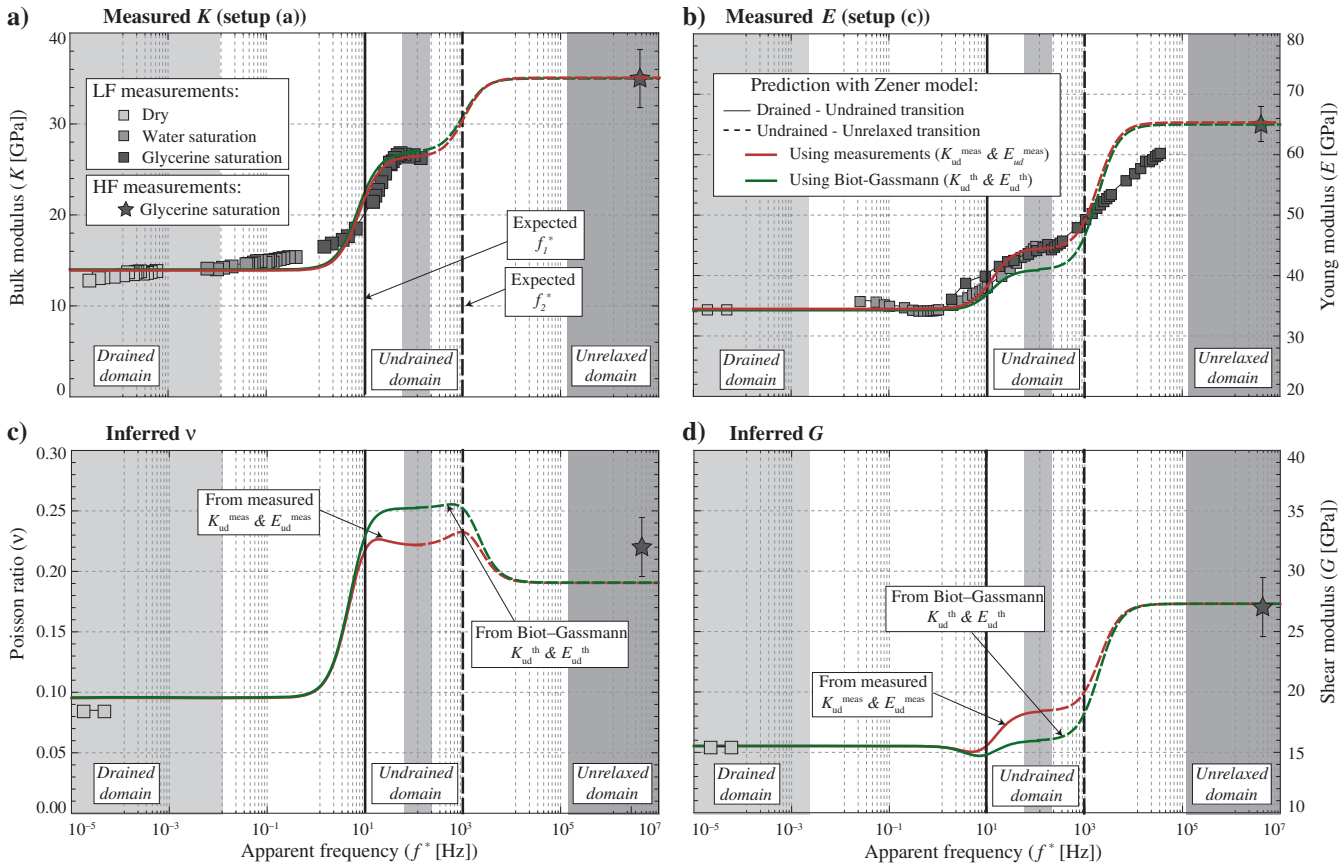

Figure 13. (a and b) Measured and (c and d) inferred elastic properties of Fo7 as a function of f^* for $P_{eff} = 1$ MPa. The measured (i.e., symbols) (a) bulk modulus (Pimienta et al., 2015) and (b) Young's modulus are compared with Zener-like predicted drained/undrained (i.e., filled curves) and undrained/unrelaxed (i.e., dashed curves) transitions. (c) Poisson's ratio and (d) shear modulus inferred from the Zener-like predictions of K and E.

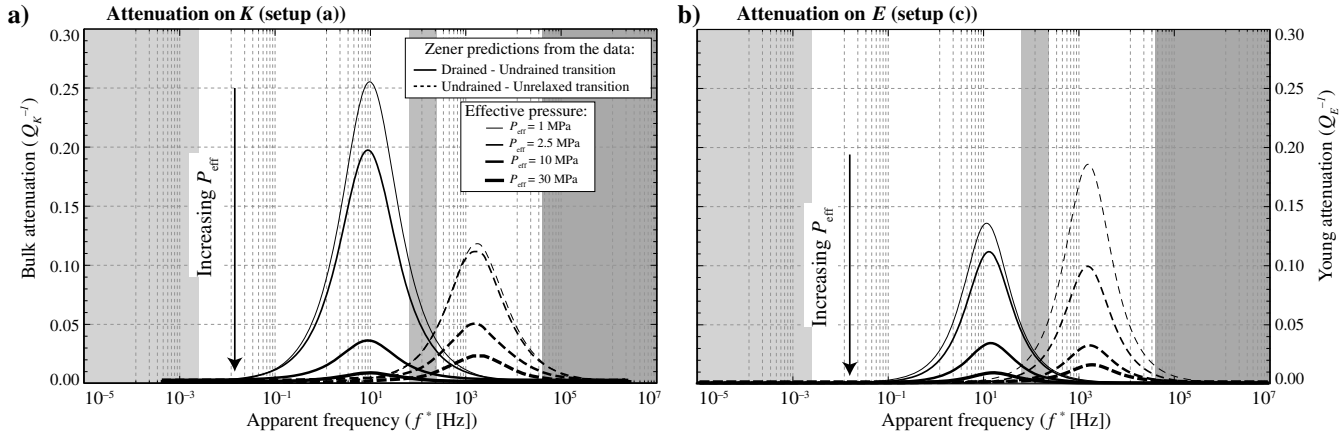

Figure 14. Comparison between the frequency-dependent attenuations on K and E for varying pressures of $P_{\text{eff}} = [1; 2.5; 10; 30]$ MPa. The attenuations are obtained using Zener model from the measured dispersions in K and E.

is again predicted to result in a large increase of G. Note that this result for the relaxed/unrelaxed transition is expected from effective medium theories for a fully saturated rock.

Both Zener plots for ν (Figure 13c) show an increase from 0.1 to 0.25 at intermediate frequencies, corresponding to the drained/undrained transition. As the frequency increases, a decrease is then inferred down to 0.19 at higher frequencies. This bell-shaped curve indicates that the undrained ν_{ud} is predicted to be higher than the unrelaxed ν_{ur}. This behavior is in fact consistent with effective medium theories calculations for a microcracked rock.

Attenuations for the different transitions

Using Zener plots fitted to the measured elastic moduli, a comparison can be proposed for ${Q_K}^{-1}$ (Figure 14a) and ${Q_E}^{-1}$ (Figure 14b) for different pressures of $P_{\text{eff}} = [1; 2.5; 10; 30]$ MPa.

Two strong attenuation peaks are predicted for ${Q_K}^{-1}$ and ${Q_E}^{-1}$ at low effective pressures. Both attenuation peaks decrease when increasing P_{eff}, which is consistent with the fact that the microcracks progressively close when increasing the confining pressure. At $P_{\text{eff}} = 1$ MPa, ${Q_K}^{-1}$ (Figure 14a) is predicted to be larger for the drained/undrained transition than for the relaxed/unrelaxed one. The reverse is predicted for ${Q_E}^{-1}$ (Figure 14a). This difference originates from the fact that E combines K and G. Because G is not expected to show any dispersion for the drained/undrained transition, ${Q_E}^{-1}$ should consistently be lower than ${Q_K}^{-1}$ for this transition.

CONCLUSION

Calibration of a new setup with two standard samples (i.e., glass and gypsum) shows that Young's modulus and Poisson's ratio can be measured in the frequency ranges of $P_c \in [0; 30]$ MPa and $f \in [510^{-3}; 10^2]$ Hz, respectively. The bulk and shear moduli can be inferred from these data. The results fit well with the previously published data. No pressure or frequency dependency of the apparatus is observed. Using the Plexiglas sample, measurements of Young's modulus dispersion and attenuation are consistent with the previous measurements. The new setup is accurate over the pressure and frequency ranges of $f \in [510^{-3}; 10^2]$ Hz, respectively.

The pressure dependence of Young's modulus has been measured at different frequencies on well-known sandstone samples saturated by water and glycerin. One sample shows small variations. The other one exhibits strong pressure- and frequency-dependent variations. This second sample has been further investigated as a function of frequency for both saturating fluids. Large frequency-dependent variations have been measured on the Young's modulus and attenuation. The key parameter for these effects, defined as the apparent frequency f^*, combines frequency and the fluids' viscosity in the same manner. Using this parameter shows that Young's modulus and attenuation have been investigated over the range of $f^* \in [10^{-3}; 10^5]$ Hz. The measurements using different fluids compare favorably, and both drained/undrained and relaxed/unrelaxed transitions have been measured. Combining the present results with previous ones on the bulk modulus, Poisson's ratio and shear modulus have been inferred over the frequency range. Poisson's ratio appears to be strongly frequency dependent and shows a large bell-shaped variation. The shear modulus shows a slight evidence of a dispersion associated with the drained/undrained transition, and a stronger variation associated with the relaxed/unrelaxed transition.

ACKNOWLEDGMENTS

This work has been partially supported by Total, under project no. FR00007429. The authors wish to thank Y. Pinquier and A. Schubnel for their technical help in setting up the measuring system. M. Lebedev, B. Quintal, and an anonymous reviewer are thanked for their constructive comments.

APPENDIX A

MEASURED HYDRAULIC CONDUCTIVITY

To understand the fluid-flow effects at the sample scales, the rocks' transport properties have to be measured. The pressure gradient method (e.g., Ougier-Simonin et al., 2011) is used here (Figure A-1a and A-1b). It consists in applying a pressure gradient (Figure A-1a) and measuring the fluid flow (Figure A-1b). Knowing

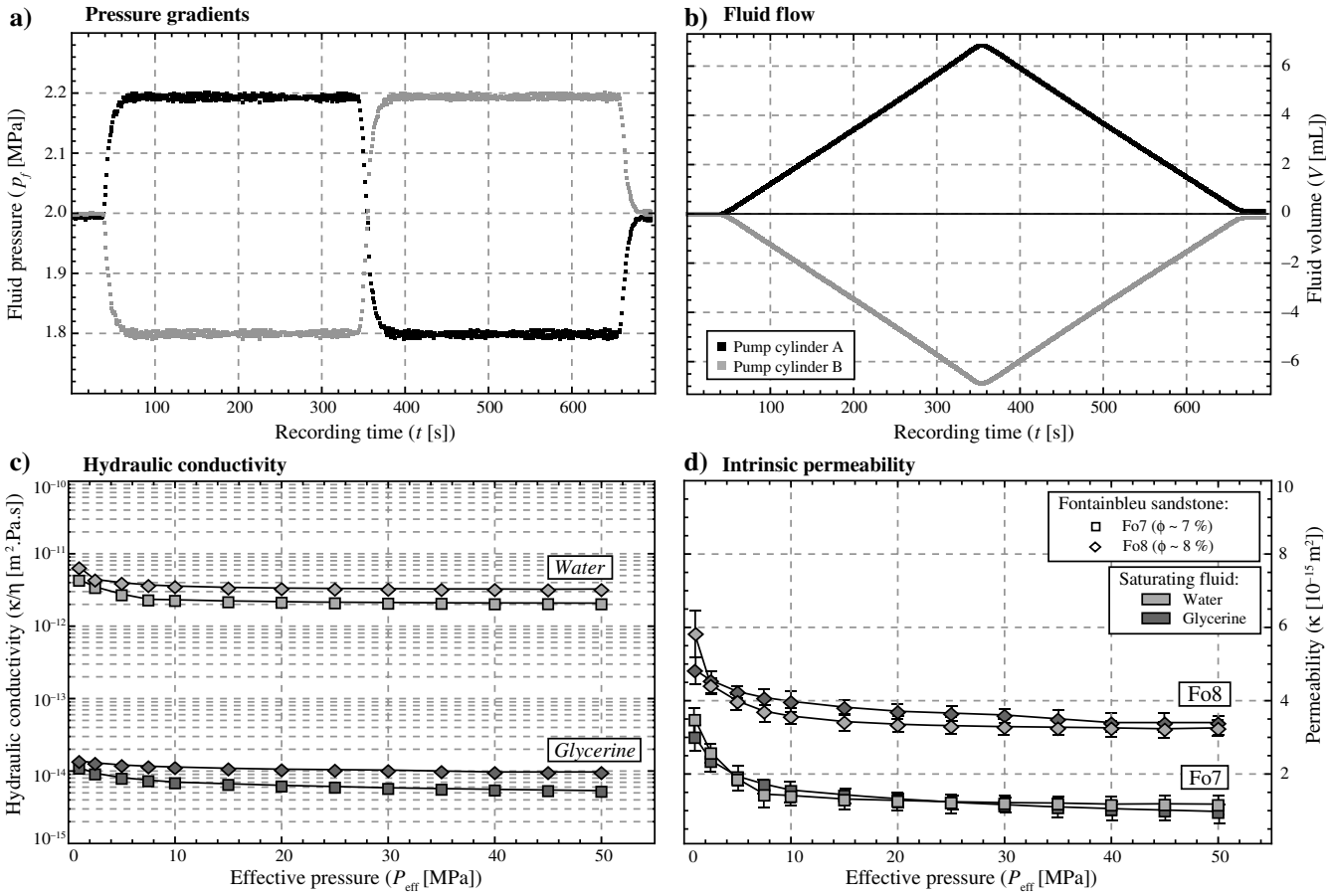

Figure A-1. Example of a permeability measurement for Fo7 by (a) applying a pressure gradient and (b) measuring the fluid flow at both ends of the sample. Here, Pump A is linked to the sample's top, and Pump B is linked to the sample's bottom. (c) Measured hydraulic conductivities as a function of effective pressure for Fo7 (i.e., squares) and Fo8 (i.e., diamonds) saturated by either water or glycerin and (d) The inferred samples' intrinsic permeabilities as a function of the effective pressure for Fo7 and Fo8. For both samples, the glycerin viscosity chosen for the fit between water and glycerin is of $\eta_{gly} = 350\eta_{wat} = 0.312$ Pa.s.

the pressure gradient and fluid flow allows one to measure the hydraulic conductivity (κ/η) across the sample, which is obtained for each confining step. The samples' hydraulic conductivities are measured for the different P_{eff} under the glycerin and water saturation (Figure A-1c). As shown from the protocol (Figure A-1a and A-1b), four values of hydraulic conductivity may be obtained from this method, so that four permeabilities may also be inferred. The reported measurements and error bars correspond to the mean and standard deviation between the four measurements (Figure A-1c and A-1d).

From the measured hydraulic conductivities, about two to three orders of magnitudes separate the water-saturated measurements from the glycerin-saturated ones (Figure A-1c). If one assumes the permeability values to be identical for both fluids (Figure A-1d), the difference between the fluids' in situ viscosities does not correspond to the theoretical ratio (i.e., $\eta_{wat}/\eta_{gly} \sim 1221$) but to the ratio $\eta_{wat}/\eta_{gly} \sim 350$. This empirical ratio between water's and glycerin's viscosities (i.e., $\eta_{gly} = 350\eta_{wat}$) is found to be the same for Fo7 and Fo8 (Figure A-1d). Another possible assumption would be that the permeability depends on the fluid nature (because, for instance, the fluid paths would be different). In any case, the relevant parameter for frequency dependence in the LF range is (κ/η) (Pimienta et al., 2015).

REFERENCES

Adam, L., M. Batzle, and I. Brevik, 2006, Gassmann's fluid substitution and shear modulus variability in carbonates at laboratory seismic and ultrasonic frequencies: Geophysics, **71**, no. 6, F173–F183, doi: 10.1190/1.2358494.

Adelinet, M., J. Fortin, Y. Guéguen, A. Schubnel, and L. Geoffroy, 2010, Frequency and fluid effects on elastic properties of basalt: Experimental investigations: Geophysical Research Letters, **37**, L02303, doi: 10.1029/2009GL041660.

Batzle, M., R. Hofmann, D.-H. Han, and J. Castagna, 2001, Fluids and frequency dependent seismic velocity of rocks: The Leading Edge, **20**, 168–171, doi: 10.1190/1.1438900.

Batzle, M. L., D.-H. Han, and R. Hofmann, 2006, Fluid mobility and frequency-dependent seismic velocity — Direct measurements: Geophysics, **71**, no. 1, N1–N9, doi: 10.1190/1.2159053.

Boudet, J., and S. Ciliberto, 1998, Interaction of sound with fast crack propagation: Physical Review Letters, **80**, 341–344, doi: 10.1103/PhysRevLett.80.341.

Bourbie, T., and B. Zinszner, 1985, Hydraulic and acoustic properties as a function of porosity in Fontainebleau sandstone: Journal of Geophysical Research: Solid Earth, **90**, 11524–11532, doi: 10.1029/JB090iB13p11524.

Brantut, N., A. Schubnel, E. David, E. Héripré, Y. Guéguen, and A. Dimanov, 2012, Dehydration-induced damage and deformation in gypsum

and implications for subduction zone processes: Journal of Geophysical Research: Solid Earth, **117**, B03205, doi: 10.1029/2011JB008730.
Cleary, M. P., 1978, Elastic and dynamic response regimes of fluid-impregnated solids with diverse microstructures: International Journal of Solids and Structures, **14**, 795–819, doi: 10.1016/0020-7683(78)90072-0.
David, E. C., J. Fortin, A. Schubnel, Y. Guéguen, and R. W. Zimmerman, 2013, Laboratory measurements of low-and high-frequency elastic moduli in Fontainebleau sandstone: Geophysics, **78**, no. 5, D369–D379, doi: 10.1190/geo2013-0070.1.
Fortin, J., Y. Guéguen, and A. Schubnel, 2007, Effects of pore collapse and grain crushing on ultrasonic velocities and V_p/V_s: Journal of Geophysical Research: Solid Earth, **112**, B08207, doi: 10.1029/2005JB004005.
Fortin, J., L. Pimienta, Y. Guéguen, A. Schubnel, E. David, and M. Adelinet, 2014, Experimental results on the combined effects of frequency and pressure on the dispersion of elastic waves in porous rocks: The Leading Edge, **33**, 648–654, doi: 10.1190/tle33060648.1.
Fortin, J., A. Schubnel, and Y. Guéguen, 2005, Elastic wave velocities and permeability evolution during compaction of Bleurswiller sandstone: International Journal of Rock Mechanics and Mining Sciences, **42**, 873–889, doi: 10.1016/j.ijrmms.2005.05.002.
Ghabezloo, S., and J. Sulem, 2010, Effect of the volume of the drainage system on the measurement of undrained thermo-poro-elastic parameters: International Journal of Rock Mechanics and Mining Sciences, **47**, 60–68, doi: 10.1016/j.ijrmms.2009.03.001.
Gomez, C., J. Dvorkin, and T. Vanorio, 2010, Laboratory measurements of porosity, permeability, resistivity, and velocity on Fontainebleau sandstones: Geophysics, **75**, no. 6, E191–E204, doi: 10.1190/1.3493633.
Jackson, I., and M. Paterson, 1987, Shear modulus and internal friction of calcite rocks at seismic frequencies: Pressure, frequency and grain size dependence: Physics of the Earth and Planetary Interiors, **45**, 349–367, doi: 10.1016/0031-9201(87)90042-2.
Madonna, C., and N. Tisato, 2013, A new seismic wave attenuation module to experimentally measure low-frequency attenuation in extensional mode: Geophysical Prospecting, **61**, 302–314, doi: 10.1111/1365-2478.12015.
Madonna, C., N. Tisato, B. Artman, and E. Saenger, 2011, Laboratory measurements of seismic attenuation from 0.01 to 100 Hz: 73rd Annual International Conference and Exhibition, EAGE, Extended Abstracts, doi: 10.3997/2214-4609.20149425.
Mallet, C., J. Fortin, Y. Guéguen, and F. Bouyer, 2013, Effective elastic properties of cracked solids: An experimental investigation: International Journal of Fracture, **182**, 275–282, doi: 10.1007/s10704-013-9855-y.
Mallet, C., J. Fortin, Y. Guéguen, and F. Bouyer, 2015, Brittle creep and subcritical crack propagation in glass submitted to triaxial conditions: Journal of Geophysical Research: Solid Earth, **120**, 879–893, doi: 10.1002/2014JB011231.
Mikhaltsevitch, V., M. Lebedev, and B. Gurevich, 2011, A low-frequency apparatus for characterizing the mechanical properties of rocks: 73rd Annual International Conference and Exhibition, EAGE, Extended Abstracts, doi: 10.3997/2214-4609.20149481.
Mikhaltsevitch, V., M. Lebedev, and B. Gurevich, 2014, A laboratory study of low-frequency wave dispersion and attenuation in water-saturated sandstones: The Leading Edge, **33**, 616–622, doi: 10.1190/tle33060616.1.
Nowick, A., and B. Berry, 1972, Anelastic relaxation in crystalline solids: Elsevier.
Ougier-Simonin, A., J. Fortin, Y. Guéguen, A. Schubnel, and F. Bouyer, 2011, Cracks in glass under triaxial conditions: International Journal of Engineering Science, **49**, 105–121, doi: 10.1016/j.ijengsci.2010.06.026.
Pimienta, L., J. Fortin, and Y. Guéguen, 2014, Investigation of elastic weakening in limestone and sandstone samples from moisture adsorption: Geophysical Journal International, **199**, 335–347, doi: 10.1093/gji/ggu257.
Pimienta, L., J. Fortin, and Y. Guéguen, 2015, Bulk modulus dispersion and attenuation in sandstones: Geophysics, **80**, no. 2, D111–D127, doi: 10.1190/geo2014-0335.1.
Sarout, J., 2012, Impact of pore space topology on permeability, cut-off frequencies and validity of wave propagation theories: Geophysical Journal International, **189**, 481–492, doi: 10.1111/j.1365-246X.2011.05329.x.
Subramaniyan, S., B. Quintal, N. Tisato, E. H. Saenger, and C. Madonna, 2014, An overview of laboratory apparatuses to measure seismic attenuation in reservoir rocks: Geophysical Prospecting, **62**, 1211–1223, doi: 10.1111/1365-2478.12171.
Tisato, N., and C. Madonna, 2012, Attenuation at low seismic frequencies in partially saturated rocks: Measurements and description of a new apparatus: Journal of Applied Geophysics, **86**, 44–53, doi: 10.1016/j.jappgeo.2012.07.008.
Wang, H. F., 2000, Theory of linear poroelasticity: Princeton University Press, Princeton Series in Geophysics.
Wang, X.-Q., A. Schubnel, J. Fortin, E. David, Y. Guéguen, and H.-K. Ge, 2012, High Vp/Vs ratio: Saturated cracks or anisotropy effects?: Geophysical Research Letters, **39**, L11307, doi: 10.1029/2012GL051742.